

# Computing extracellular electrical potentials from neuronal simulations

Geir Halnes<sup>a,b</sup>, Torbjørn V. Ness<sup>a</sup>, Solveig Næss<sup>b</sup>, Klas H. Pettersen<sup>c</sup>, Gaute T. Einevoll<sup>a,b,d,\*</sup>

<sup>a</sup>*Faculty of Science and Technology, Norwegian University of Life Sciences, Ås, Norway*

<sup>b</sup>*Center for Integrative Neuroplasticity, University of Oslo, Oslo, Norway*

<sup>c</sup>*Norwegian Artificial Intelligence Research Consortium, Oslo, Norway*

<sup>d</sup>*Department of Physics, University of Oslo, Oslo, Norway*

---

## Abstract

Measurements of electric potentials from neural activity have played a key role in neuroscience for almost a century, and simulations of neural activity is an important tool for understanding such measurements. Volume conductor (VC) theory is used in neuroscience to compute extracellular electrical potentials such as extracellular spikes, MUA, LFP, ECoG and EEG, and also during analysis of recorded potentials for reconstructing the neuronal current sources through current source density methods. In this book chapter, we show how VC theory can be derived from a detailed electrodiffusive theory for ion concentration dynamics in the extracellular medium, and show what assumptions that must be introduced to get the VC theory on the simplified form that is commonly used by neuroscientists. Furthermore, we provide examples of how the theory is applied, using the Python tool LFPy [TVN: jeg pleier å tenke at de nevnte spesifikke simulatorer er for detaljert for abstracts?] to compute spikes, LFP signals and EEG signals generated by neurons and neuronal populations.

**Keywords:** extracellular potentials, LFP, EEG, ECoG, electrodiffusion, neuronal simulation

---

## Contents

<b>1</b>	<b>Introduction</b>	<b>2</b>
<b>2</b>	<b>From electrodiffusion to volume conductor theory</b>	<b>3</b>
2.1	Ion concentration dynamics . . . . .	4
2.2	Electrodynamics . . . . .	5
2.3	Volume conductor theory . . . . .	6
2.3.1	Current-dipole approximation . . . . .	7
2.3.2	Assumptions in volume conductor theory . . . . .	8
2.4	Modeling electrodes . . . . .	9
<b>3</b>	<b>Single-cell contributions to extracellular potentials</b>	<b>10</b>

---

\*correspondence: [gaute.einevoll@nmbu.no](mailto:gaute.einevoll@nmbu.no)

<b>4</b>	<b>Intra-cortical extracellular potentials from neural populations</b>	<b>10</b>
4.1	Local field potentials . . . . .	11
4.2	MUA . . . . .	13
<b>5</b>	<b>ECoG and EEG</b>	<b>13</b>
5.1	Head models . . . . .	14
<b>6</b>	<b>Discussion</b>	<b>15</b>

## 1. Introduction

Arguably, most of what we have learned about the mechanisms by which neurons and networks operate in living brains comes from recordings of extracellular potentials. In such recordings, electrical potentials are measured by electrodes that are either placed between cells in brain tissue (spikes, LFPs), at the cortical surface (ECoG, electrocorticography), or at the scalp (EEG, electroencephalography) (Figure 1). Spikes, the high-frequency part of the extracellular potentials recorded inside gray matter, are reliable signatures of neuronal action potentials, and spike measurements have been instrumental in mapping out, for example, receptive fields accounting for how sensory stimuli are represented in the brain. The analysis of the LFP signal, the low-frequency part of electrical potentials recorded inside gray matter, as well as the ECoG, and EEG signals is less straightforward. Interpretation of the signal in terms of the underlying neural activity has been difficult, and most analysis of the data has been purely statistical [Nunez and Srinivasan, 2006; Buzsáki et al., 2012; Einevoll et al., 2013a; Ilmoniemi and Sarvas, 2019].

The tradition of physics is different. Here candidate hypotheses are typically formulated as specific mathematical models, and predictions computed from the models are compared with experiments. In neuroscience this approach has been used to model activity in individual neurons using, for example, biophysically detailed neuron models based on the cable equation formalism (see, e.g., Koch [1999]; Sterratt et al. [2011]). Here the models have largely been developed and tested by comparison with membrane potentials recorded by intracellular electrodes in *in vitro* settings (but see Gold et al. [2007]). To pursue this mechanistic approach to network models in layered structures such as cortex or hippocampus, one would like to compare model predictions with all available experimental data, that is, not only spike times recorded for a small subset of the neurons, but also population measures such as LFP, ECoG and EEG signals [Einevoll et al., 2019]. This chapter addresses how to model such electrical population signals from neuron and network models.

In addition to allowing for validation on large-scale network models mimicking specific biological networks, e.g., Reimann et al. [2013]; Markram et al. [2015]; Billeh et al. [2020], we believe a key application is to generate model-based benchmarking data for validation of data analysis methods [Denker et al., 2012]. One example is the use of such benchmarking data to develop and test spike-sorting methods Hagen et al. [2016]; Buccino and Einevoll [2019] or test methods for localization and classification of cell types [Delgado Ruz and Schultz, 2014; Buccino et al., 2018]. Another example is testing of methods for analysis of LFP signals, such as CSD analysis [Pettersen et al., 2008; Łęski et al., 2011; Ness et al., 2015] or ICA analysis [Głabska et al., 2014], or joint analysis of spike and LFP signals such as laminar population analysis (LPA) [Głabska et al., 2016].

The standard way to compute extracellular potentials from neural activity is a two-step process [Holt and Koch, 1999; Lindén et al., 2014; Hagen et al., 2018]:

- 36     1. Compute the net transmembrane current in all neuronal segments in (networks of) biophysically-  
 37       detailed neuron models, and  
 38     2. use volume-conductor (VC) theory to compute extracellular potentials from the these com-  
 39       puted transmembrane currents.

40 This book chapter describes the origin of VC theory, that is, how it can be derived from a more de-  
 41 tailed electrodiffusive theory describing dynamics of ions in the extracellular media. It also provides  
 42 examples where our tool LFPy ([LFPy.github.io](https://LFPy.github.io)) [[Lindén et al., 2014](#); [Hagen et al., 2018](#)] is used  
 43 to compute spikes, LFP signals and EEG signals generated by neurons and neuronal populations.

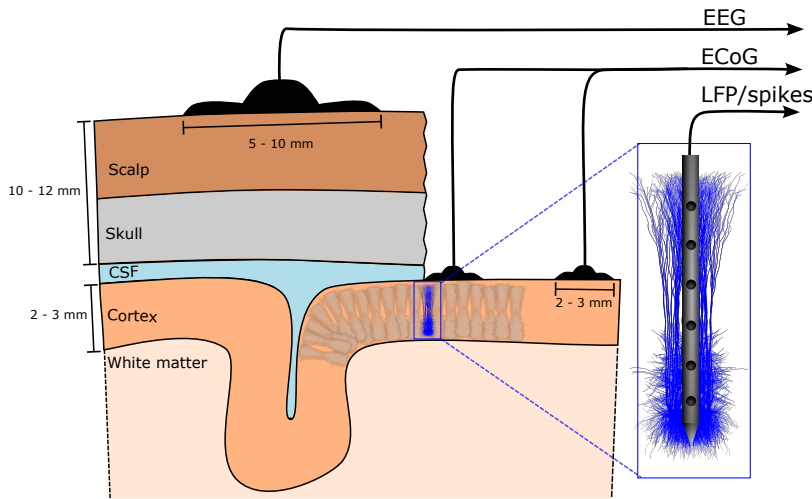


Figure 1: **LFP, ECoG and EEG.** The same basic building blocks, that is, currents caused by large numbers of synaptic input are contributing to several different measurable signals.

## 44 2. From electrodiffusion to volume conductor theory

45 The recorded extracellular potentials are generated by electrical currents, that is, movement  
 46 of ions, in the extracellular space. Such an extracellular electrical current can in principle include  
 47 several components:

- 48     1. a drift component (ions migrating in electrical fields),  
 49     2. a diffusion component (ions diffusing due to concentration gradients),  
 50     3. an advective component (extracellular fluid flow drags ions along), and  
 51     4. a displacement component (ions pile up and changes the local charge density).

52 Since the extracellular bulk fluid has very fast relaxation times and is very close to electroneutral,  
 53 the latter two current components (3-4) are extremely small and are typically neglected [[Grodzinsky,](#)  
 54 [Gratiy et al., 2017](#)]. The diffusive component (2) is acknowledged to play an important role for  
 55 voltage dynamics on a tiny spatial scale, such as in synaptic clefts or in the close vicinity of neuronal

membranes, where ion concentrations can change dramatically within very short times [Savchenko et al., 2017; Pods, 2017]. At macroscopic tissue level, it is commonly believed that the diffusive current is much smaller than the drift current, so that even diffusive currents are typically neglected so that only the drift component (1) is considered. Then the extracellular medium is considered to be a volume conductor (VC) which greatly simplifies the calculation of extracellular potentials [Holt and Koch, 1999; Lindén et al., 2014].

However, if large ion-concentration gradients are present, diffusive currents could in principle affect measurable extracellular potentials [Halnes et al., 2016, 2017; Solbrå et al., 2018]. Thus in scenarios involving dramatic shifts in extracellular concentrations, such as spreading depression and related pathologies, diffusive effects are likely to be of key importance for shaping the extracellular potential [Almeida et al., 2004; O'Connell and Mori, 2016]. If so, VC theory is insufficient, and computationally much more expensive electrodiffusive modeling must be used instead.

In this section we start with a very general assumption of how ions moving through the brain under the combined influence of electric fields and concentration gradients TVN: strange sentence? . Building on this, we then first describe several computational schemes for modelling electrodiffusive processes before we derive the fundamental equations for VC theory assuming negligible effects from diffusion.

### 2.1. Ion concentration dynamics

The movement of ions, that is, charged atoms or molecules, in the brain are described in terms of the flux, and there are essentially two different processes that cause ions to move in the brain, namely diffusion and electrical drift. In such electrodiffusive processes, the flux density of an ion species  $k$  is given by [Koch, 1999]:

$$\mathbf{j}_k = -D_k \nabla c_k - \frac{D_k z_k c_k}{\psi} \nabla \phi, \quad (1)$$

where the first term on the right is Fick's law for the diffusive flux density  $j_k^{\text{diff}}$ , and the second term is the drift flux density  $j_k^{\text{drift}}$ , which expands Fick's law in the case where the diffusing particles also move due to electrostatic forces with a mobility  $D_k/\psi$  (cf. the Einstein-relation, Mori et al. [2008]). Here  $D_k$  is the diffusion coefficient of ion species  $k$ ,  $\phi$  is the electric potential,  $z_k$  is the valency of ion species  $k$ , and  $\psi = RT/F$  is defined by the gas constant ( $R$ ), Faraday's constant ( $F$ ) and the temperature ( $T$ ). The ion concentration dynamics of a given species is then given by the Nernst-Planck continuity equation:

$$\frac{\partial c_k}{\partial t} = -\nabla \cdot \mathbf{j}_k + f_k = \nabla \cdot \left[ D_k \nabla c_k + \frac{D_k z_k c_k}{\psi} \nabla \phi \right] + f_k \quad (2)$$

where  $f_k$  represents any source term in the system, such as e.g., an ionic transmembrane current source [Solbrå et al., 2018].

In order to solve a set (i.e., one for each ion species present) of equations like eq. 2, one needs an expression for the electrical potential  $\phi$ . There are two main approaches to this. The physically most detailed approach is to use the Poisson-Nernst-Planck (PNP) formalism [Léonetti and Dubois-Violette, 1998; Léonetti et al., 2004; Lu et al., 2007; Lopreore et al., 2008; Nanninga, 2008; Pods

91 et al., 2013; Gardner et al., 2015]. Then  $\phi$  is determined from Poisson's equation from electrostatics,

92

$$\nabla^2\phi = -\rho/\epsilon, \quad (3)$$

93 where  $\epsilon$  is the permittivity of the system, and  $\rho$  is the charge density associated with the ionic  
94 concentrations, as given by:

$$\rho = F \sum_k z_k c_k. \quad (4)$$

95 An alternative, more computationally efficient approach is to replace the Poisson equation with the  
96 simplifying approximation that the bulk solution is electroneutral [Mori et al., 2008; Mori, 2009; Mori  
97 and Peskin, 2009; Mori et al., 2011; Haines et al., 2015, 2013; Pods, 2017; Niederer, 2013; O'Connell  
98 and Mori, 2016; Solbrå et al., 2018; Ellingsrud et al., 2020], which is a good approximation on  
99 spatiotemporal scales larger than micrometers and microseconds [Grodzinsky, 2011; Pods, 2017;  
100 Solbrå et al., 2018].

101 Both the PNP formalism and the electroneutral formalism allow us to compute the dynamics of  
102 ion concentrations and the electrical potential in the extracellular space of neural tissue containing  
103 an arbitrary set of neuronal and glial current sources. For example, in recent work, a version  
104 of the electroneutral formalism called the Kirchhoff-Nernst-Planck (KNP) formalism was developed  
105 into a framework for computing the extracellular dynamics (of  $c_k$  and  $\phi$ ) in a 3D space surrounding  
106 morphologically complex neurons simulated with the NEURON simulation tool [Solbrå et al., 2018].  
107 However, both the PNP and electroneutral formalisms such as KNP keep track of the spatial dis-  
108 tribution of ion concentrations, and as such they require a suitable meshing of the 3D space, and  
109 numerical solutions based on finite difference- or finite element methods. In both cases, simulations  
110 can become very heavy, and for systems at a tissue level the required computational demand may  
111 be too large to be feasible. For that reason, there is much to gain from deriving a simpler frame-  
112 work where effects of ion concentration dynamics are neglected, since, for many scenarios, this may  
113 be a good approximation. Below, we will derive this simpler frameworks, i.e., the standard volume  
114 conductor (VC) theory, using the Nernst-Planck fluxes (eq. 1) as a starting point.

115 *2.2. Electrodynamics*

116 If we multiply eq. 1 by  $F \cdot z_k$  and take the sum over all ion species, we get an expression for the  
117 net electrical current density due to all particle fluxes:

$$\mathbf{i} = - \sum_k F z_k D_k \nabla c_k - \sigma \nabla \phi \quad (5)$$

118 where the first term is the diffusive current density  $i^{\text{diff}}$  and the second term is the drift current density  
119  $i^{\text{drift}}$ . We have here identified the conductivity  $\sigma$  of the medium as [Koch, 1999]:

$$\sigma = F \sum_k \frac{\tilde{D}_k z_k^2}{\psi} c_k. \quad (6)$$

120 Current conservation in the extracellular space implies that:

$$\nabla \cdot \mathbf{i} = - \sum_k F z_k D_k \nabla^2 c_k - \nabla \cdot (\sigma \nabla \phi) = -C, \quad (7)$$

121 where  $C$  denotes the current source density (CSD), reflecting e.g., local neuronal or glial transmembrane currents. We note that this is essentially equivalent to eq. 2 at the level of single ion species,  
 122 with the exception that eq. 2 contains a term  $\partial c_k / \partial t$  for accumulation of ion species  $k$ , while eq. 7  
 123 does *not* contain a corresponding term  $(\partial \rho / \partial t)$  for charge accumulation. Hence, in eq. 7 it is im-  
 124 plicitly assumed that the extracellular bulk solution is electroneutral [Solbrå et al., 2018]. We note  
 125 that in general, the *CSD* term includes both ionic transmembrane currents and transmembrane  
 126 capacitive currents, and that the latter means that the local charge accumulation building up the  
 127 transmembrane potential still occurs in the membrane Debye-layer.

128 Note that if we assume all concentrations to be constant in space, the diffusive term vanishes,  
 129 and eq. 7 reduces to:

$$\nabla \cdot (\sigma \nabla \phi) = -C. \quad (8)$$

130 This the standard expression used in CSD theory [Mitzdorf, 1985; Nicholson and Freeman, 1975;  
 131 Pettersen et al., 2006], where spatially distributed recordings of  $\phi$  are used to make theoretical pre-  
 132 dictions of underlying current sources. When using eq. 8, it is implicitly assumed that the Laplacian  
 133 of  $\phi$  exclusively reflects transmembrane current sources, and that it is not contributed to by diffusive  
 134 processes.

135 We note there are two conventions for defining the variables in eqns. 1-8, both of which are  
 136 in use. The variables can be defined either relative to a tissue reference volume or relative to an  
 137 extracellular reference volume. The former convention is the common convention used in volume  
 138 conductor theory. Then concentrations denote the number of extracellular ions per unit tissue vol-  
 139 ume, sources denote the number of ions/the net charge per unit tissue volume per second, and  
 140 flux/current densities are defined per unit tissue cross-section area. Then,  $\sigma$  interprets as the con-  
 141 ductivity experienced by the current density per tissue cross section area.

142 As eq. 7 indicates, also diffusive processes can in principle contribute to the Laplacian of  $\phi$ , and  
 143 if present, they could give rise to a non-zero Laplacian of  $\phi$  even in the absence of neuronal sources  
 144 ( $C = 0$ ). Previous computational studies have predicted that effects of diffusion on extracellular po-  
 145 tentials are not necessarily small, but tend to be very slow, meaning that they will only affect the very  
 146 low-frequency components of  $\phi$  [Halnes et al., 2016, 2017]. This is due to the diffusive current being  
 147 a direct function of ion concentrations  $c_k$ , which on a large spatial scale typically vary on a much  
 148 slower time scale (seconds-minutes) than the fluctuations in  $\phi$  that we commonly are interested  
 149 in (milliseconds-seconds). Furthermore, electrodes used to record  $\phi$  typically have a lower cutoff  
 150 frequency of 0.1-1 Hz [Einevoll et al., 2013a], which means that most of the tentative diffusive con-  
 151 tribution will be filtered out from experimental recordings. It may therefore be a good approximation  
 152 to neglect the diffusive term, except in the case of pathologically dramatic concentration variations.  
 153 For the rest of this chapter, we shall do so, and assume that electrodynamics in neural tissue can be  
 154 determined by eq. 8.

### 155 2.3. Volume conductor theory

156 In simulations of morphologically complex neurons, we typically compute a set of transmem-  
 157 brane current sources for each neuronal segment [Koch, 1999]. Commonly, one assumes that the  
 158 extracellular potential does not affect the neurons (i.e., no ephaptic coupling), since extracellular  
 159 potentials are typically much smaller than the membrane potential of  $\sim 70$  mV. By assuming that  
 160 the tissue medium can be approximated as a volume conductor [Holt and Koch, 1999; Lindén et al.,

[2014], one can then use the standard CSD equation (eq. 8) to perform a forward modeling of the extracellular potential at each point in space surrounding the neuron(s).

If we consider the simple case of a single point-current source  $I_1$  at the origin in an isotropic medium, the current density  $\mathbf{i} = -\sigma \nabla \phi$  through a spherical shell with area  $4\pi r^2$  must, due to the spherical symmetry, equal  $I_1/4\pi r^2 \hat{\mathbf{r}}$ . Integration with respect to  $r$  gives us:

$$\phi = \frac{I_1}{4\pi\sigma r}, \quad (9)$$

where  $r$  is the distance from the source.

If we have several point-current sources,  $I_1, I_2, I_3, \dots$ , in locations  $\mathbf{r}_1, \mathbf{r}_2, \mathbf{r}_3, \dots$ , their contributions add up due to the linearity assumption (see sec. 2.3.2), and the potential in a point  $\mathbf{r}$  is given by:

$$\phi(\mathbf{r}) = \frac{I_1}{4\pi\sigma|\mathbf{r} - \mathbf{r}_1|} + \frac{I_2}{4\pi\sigma|\mathbf{r} - \mathbf{r}_2|} + \frac{I_3}{4\pi\sigma|\mathbf{r} - \mathbf{r}_3|} + \dots = \sum_k \frac{I_k}{4\pi\sigma|\mathbf{r} - \mathbf{r}_k|}. \quad (10)$$

Eq. 10 is often referred to as the point-source approximation [Holt and Koch, 1999; Lindén et al., 2014], since the membrane current from a neuronal segment is assumed to enter the extracellular medium in a single point. An often used further development is obtained by integrating eq. 10 along the segment axis, corresponding to the transmembrane current being evenly distributed along the segment axis, giving the line-source approximation [Holt and Koch, 1999; Lindén et al., 2014].

### 2.3.1. Current-dipole approximation

When estimating the extracellular potential far away from a volume containing a combination of current sinks and sources, it can often be useful to express eq. (10) in terms of a multipole expansion. That is,  $\phi$  can be precisely described by [Nunez and Srinivasan, 2006],

$$\phi(R) = \frac{C_{\text{monopole}}}{R} + \frac{C_{\text{dipole}}}{R^2} + \frac{C_{\text{quadrupole}}}{R^3} + \frac{C_{\text{octupole}}}{R^4} + \dots, \quad (11)$$

when the distance  $R$  from the center of the volume to the measurement point is larger than the distance from volume center to the most peripheral source [Jackson, 1998].

In neural tissue, there will be no current monopole contribution to the extracellular potential, that is,  $C_{\text{monopole}} = 0$ . This follows from the requirement inherent in the cable equation that the sum over all transmembrane currents, including the capacitive currents, across the neuronal surface has to be zero at all points in time [Pettersen et al., 2012]. Further, the quadrupole, octupole and higher-order contributions decay rapidly with distance  $R$ . Consequently, the multipole expansion can be approximated by the dipole contribution for large distances, a simplification known as the current-dipole approximation [Nunez and Srinivasan, 2006]:

$$\phi(\mathbf{R}) \approx \frac{C_{\text{dipole}}}{R^2} = \frac{1}{4\pi\sigma} \frac{|\mathbf{p}| \cos \theta}{R^2}. \quad (12)$$

Here,  $\mathbf{p}$  is the current dipole moment and  $\theta$  is the angle between the current dipole moment and the distance vector  $\mathbf{R}$ . The current dipole moment can be found by summing up all the position-weighted transmembrane currents from a neuron [Pettersen et al., 2008, 2014; Nunez and Srinivasan, 2006]:

$$\mathbf{p} = \sum_{k=1}^N I_k \mathbf{r}_k. \quad (13)$$

192 In the case of a two-compartment neuron model (see Section 3) with a current sink  $-I$  at location  
193  $\mathbf{r}_1$  and a current source  $I$  at location  $\mathbf{r}_2$ , the current dipole moment can be formulated as  $\mathbf{p} =$   
194  $-I\mathbf{r}_1 + I\mathbf{r}_2 = I(\mathbf{r}_2 - \mathbf{r}_1) = Id$ , where  $d$  is the distance vector between the current sink and the  
195 current source, giving the dipole length  $d$  and direction of the current dipole. The current-dipole  
196 approximation is applicable in the far-field limit, that is when  $R$  is much larger than the dipole length.  
197 For an investigation of the applicability of this approximation for the LFP generated by a single  
198 neuron, see [Lindén et al. \[2010\]](#).

199

200 *2.3.2. Assumptions in volume conductor theory*

201 The point-source approximation, eq. 10 (or the line-source version of it), and the current-dipole  
202 approximation, eq. (12), represent volume conductor theory in its simplest form, and are based on a  
203 set of assumptions, some of which may be relaxed for problems where it is relevant:

- 204 1. **Quasi-static approximation of Maxwell's equations:** Terms with time derivatives of the  
205 electrical and magnetic fields are neglected. This approximation appears to be well-justified  
206 for the relatively low frequencies relevant for brain signals, below about 10 kHz [[Nunez and](#)  
207 [Srinivasan, 2006](#)].
- 208 2. **Linear extracellular medium:** Linear relationship ( $\mathbf{i} = -\sigma\nabla\phi$ ) between the current density  
209  $\mathbf{i}$  and the electrical field,  $\nabla\phi$ . This is essentially Ohm's law for volume conductors, and the  
210 relation is constitutive, meaning that it is observed in nature rather than derived from any  
211 physical principle [[Nunez and Srinivasan, 2006](#); [Pettersen et al., 2012](#)].
- 212 3. **Frequency-independent conductivity:** Capacitive effects in neural tissue are assumed to be  
213 negligible compared to resistive effects in volume conduction. This approximation seems to be  
214 justified for the relevant frequencies in extracellular recordings [[Logothetis et al., 2007](#); [Miceli](#)  
215 [et al., 2017](#); [Ranta et al., 2017](#)], see Fig. 2. Note that it is possible to expand the formalism to  
216 include a frequency-dependent conductivity [[Tracey and Williams, 2011](#); [Miceli et al., 2017](#)].
- 217 4. **Isotropic conductivity:** The electrical conductivity,  $\sigma$ , is assumed to be the same in all spatial  
218 directions. Cortical measurements have indeed found the conductivities to be comparable  
219 across different lateral directions in cortical grey matter [[Logothetis et al., 2007](#)]. However,  
220 the conductivity in the depth direction, i.e., parallel to the long apical dendrites, was found  
221 to be up to 50% larger than in the lateral direction in rat barrel cortex [[Goto et al., 2010](#)].  
222 Anisotropic electrical conductivities have also been found in other brain regions, for example in  
223 frog cerebellum [[Nicholson and Freeman, 1975](#)] and in guinea-pig hippocampus [[Holsheimer,](#)  
224 [1987](#)]. The approximation that  $\sigma$  is homogeneous is still often acceptable, as it normally  
225 gives fairly good estimations of the extracellular potential, at least in cortical tissue [[Ness](#)  
226 [et al., 2015](#)]. However, it is relatively straightforward to expand the formalism to account for  
227 anisotropic conductivities [[Ness et al., 2015](#)].
- 228 5. **Homogeneous conductivity:** The extracellular medium was assumed to have the same con-  
229 ductivity everywhere. Although neural tissue is highly non-homogeneous on the micrometer  
230 scale [[Nicholson and Syková, 1998](#)], microscale inhomogeneities may average out on a larger  
231 spatial scale, and a homogeneous conductivity seems to be a reasonable approximation within  
232 cortex [[Logothetis et al., 2007](#)]. In hippocampus, however, the conductivity has been found  
233 to be layer-specific [[López-Aguado et al., 2001](#)]. In situations where the assumption of a

homogeneous conductivity is not applicable, eq. 8 can always be solved for arbitrarily complex geometries using numerical methods, like the Finite Element Method (FEM) [Logg et al., 2012]. For some example neuroscience applications, see Moffitt and McIntyre [2005]; Frey et al. [2009]; Joucla and Yvert [2012]; Haufe et al. [2015]; Ness et al. [2015]; Buccino et al. [2019]; Obien et al. [2019]. For some simple non-homogeneous cases analytical solutions can still be obtained, for example through the Method of Images for *in vitro* brain slices [Ness et al., 2015], and the four-sphere head model for EEG signals (Sec. 5) [Næss et al., 2017].

6. **No effects from ion diffusion:** To account for diffusion of ions, one would need to compute the electrodynamics of the system using one of the electrodiffusive frameworks presented in Section 2.1.

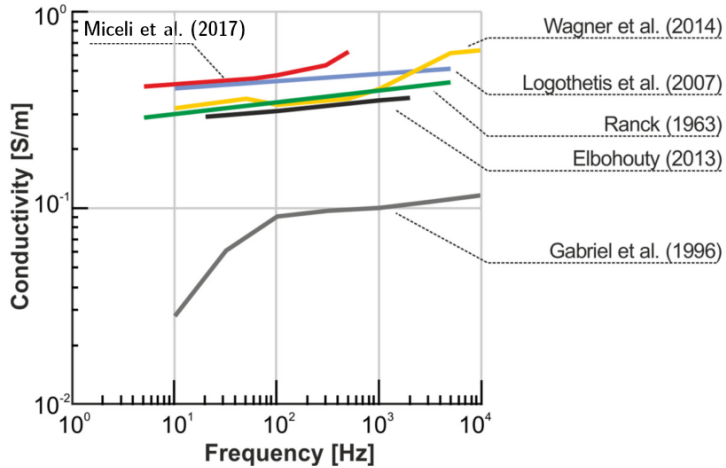


Figure 2: **Literature review of reported conductivities in various species and experimental setups.** Most studies seem to indicate a very weak frequency dependence of the extracellular conductivity, which would have a negligible effect on measured extracellular potentials [Miceli et al., 2017]. The very low and strongly frequency dependent values measured by Gabriel et al. [1996] represents an outlier, and although it has received substantial attention, it has to the best of our knowledge not been reproduced by any other study. For details about the data, see [Miceli et al., 2017], and references therein [Ranck, 1963; Gabriel et al., 1996; Logothetis et al., 2007; Elbohouty, 2013; Wagner et al., 2014].

Volume conductor theory is the fundament for forward modeling of extracellular potentials at different spatial scales, from extracellular spikes, LFPs and MUAs, to ECoGs and EEGs. In the following sections we shall review previous modeling works, and insights from simulating electrical potentials at these different scales. We use the software LFPy [Lindén et al., 2014; Hagen et al., 2018, 2019], which has volume conductor theory incorporated and can in principle be used to compute extracellular potentials on arbitrarily large spatial scales, surrounding arbitrarily large neuronal populations.

#### 2.4. Modeling electrodes

The simplest and most commonly used approach when modeling extracellular recordings is to calculate the extracellular potential at single points following one of the approaches outlined above,

254 and use this as a measure of recorded potentials. Implicitly, this assumes ideal point electrodes,  
255 that is, that the electrodes (and electrode shank) do not affect the extracellular potential and that  
256 the extracellular potential does not vary substantially over the surface of the electrodes. (This point-  
257 electrode assumption was used for all simulation examples in this chapter).

258 A numerically straightforward extension is the disc-electrode approximation where the potential  
259 is evaluated at a number of points on the electrode surface, and the average calculated [Nunez  
260 and Srinivasan, 2006; Lindén et al., 2014]. GTE: Does Nunez talk about this? TVN: Yes,  
261 eq. (5.30) in the book, however, strangely they actually use a volume integral, so maybe just re-  
262 move the reference? This approach takes into account the physical extent of the electrode, but not  
263 any effect the electrode itself might have on the electric potential. Close to the electrode surface  
264 the electric potential will however be affected by the presence of the high-conductivity electrode  
265 contact [McIntyre and Grill, 2001; Moulin et al., 2008], and a third, and numerically much more  
266 comprehensive approach to modeling electrodes is to use the Finite Element Method (FEM) to  
267 model the electrode [Moulin et al., 2008; Ness et al., 2015], or the electrode shank [Moffitt and  
268 McIntyre, 2005; Buccino et al., 2019]. Using FEM for validation, Ness et al. [2015] found that the ideal  
269 point-electrode and disc-electrode approximations were reasonably accurate when the distance  
270 between the current sources and the recording electrode was bigger than  $\sim$ 4 times and  $\sim$ 2 times the  
271 electrode radius, respectively, indicating that the effects of the electrodes themselves are negligible  
272 in most cases [Nelson and Pouget, 2010]. The presence of large multi-contact electrode probes  
273 can, however, substantially affect the extracellular potential in its vicinity, by effectively introducing a  
274 large non-conducting volume [Mechler and Victor, 2012], and this can amplify or dampen recorded  
275 potentials from nearby cells by almost a factor of two, depending on whether the cell is in front of or  
276 behind the electrode shank [Buccino et al., 2019].

277 Note that for modelling current stimulation electrodes (as opposed to just recording electrodes),  
278 more complex electrode models might be needed due to electrode polarization effects [McIntyre and  
279 Grill, 2001; Martinsen and Grimnes, 2008; Joucla and Yvert, 2012].

### 280 3. Single-cell contributions to extracellular potentials

281 The transmembrane currents of a neuron during any neural activity can be used to calculate  
282 extracellular potentials, by applying the formalism described in Sec. 2.3, and in the simplest case  
283 eq. 10. Current conservation requires that the transmembrane currents across the entire cellular  
284 membrane at any given time sum to zero [Koch, 1999; Nunez and Srinivasan, 2006], and since  
285 an excitatory synaptic input generates a current sink (negative current), this will necessarily lead to  
286 current sources elsewhere on the cell. This implies that point neurons, that is, neurons with no spatial  
287 structure, will have no net transmembrane currents, and hence cause no extracellular potentials  
288 (Fig. 3A). The simplest neuron models that are capable of producing extracellular potentials are  
289 therefore two-compartment models, which will have two equal but opposite transmembrane currents,  
290 giving rise to perfectly symmetric extracellular potentials (Fig. 3B).

291 Multi-compartment neuron models mimicking the complex spatial structure of real neurons will  
292 typically give rise to complicated patterns of current sinks and sources (negative and positive cur-  
293 rents respectively), leading to complex, but mostly dipolar-like extracellular potentials (Fig. 3C)  
294 [Einevoll et al., 2013a]. Note that this framework for calculating extracellular potentials is valid both

295 for subthreshold and suprathreshold neural activity, that is, when a cell receives synaptic input that  
 296 does not trigger, or does trigger an action potential, respectively (Fig. 3, D versus E).

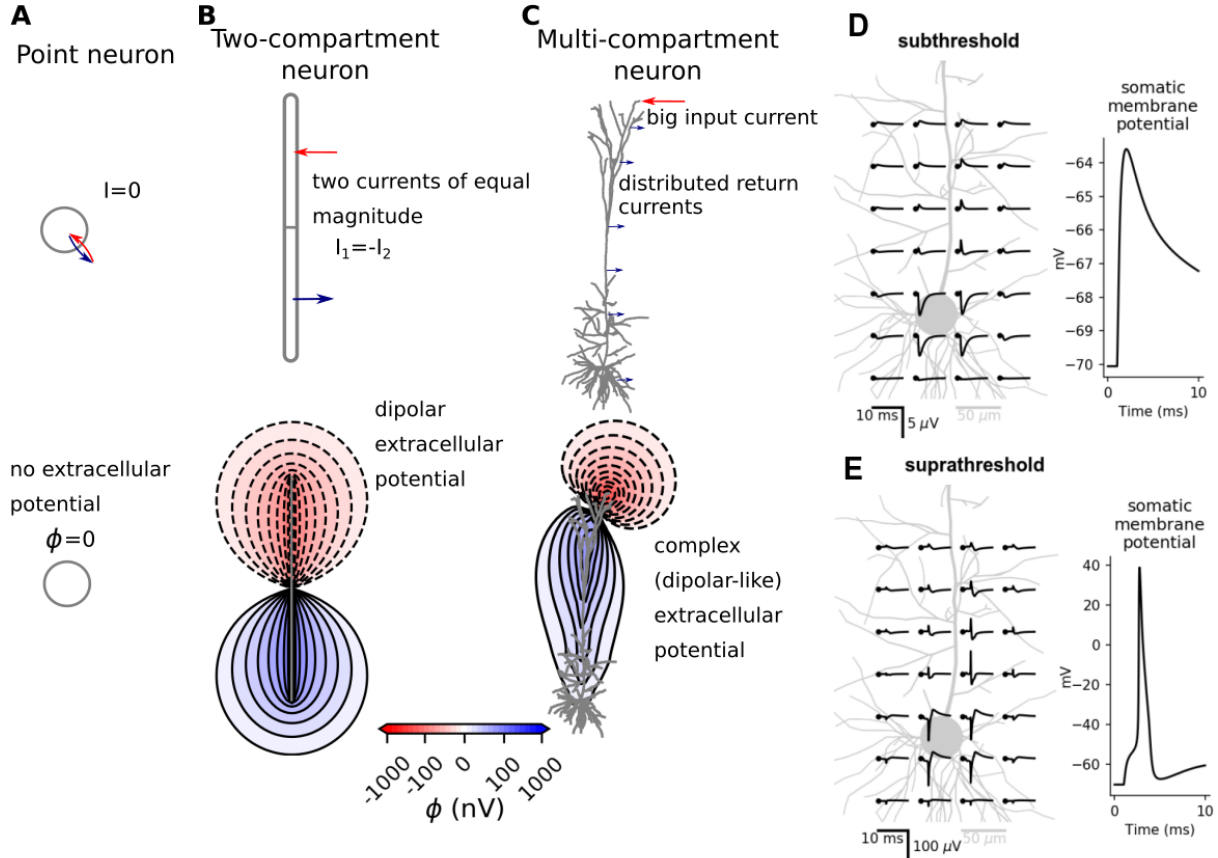
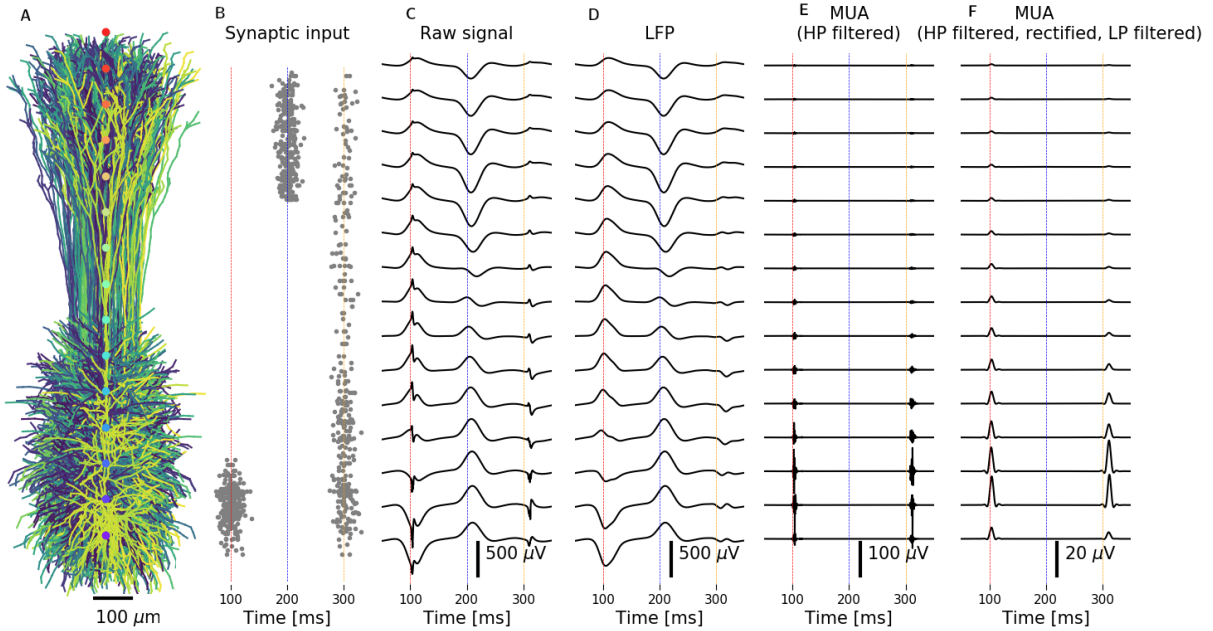


Figure 3: **Single-cell contributions to the extracellular potential.** **A:** Point neurons have no net currents (top), and therefore cause no extracellular potentials (bottom). **B:** Two-compartment neuron models have two opposite currents of identical magnitude (top), and cause perfectly symmetric dipolar-like extracellular potentials (bottom). **C:** Multi-compartment neuron models [Hay et al., 2011] give rise to complex source-sink patterns (top) and complex (but mostly dipolar-like) extracellular potentials (bottom). **D, E:** A single somatic synaptic input to a complex multi-compartment cell model, either subthreshold (D) or suprathreshold (E; double synaptic weight of D), illustrating that the same framework can be used to calculate both the LFP contribution from subthreshold synaptic input, and extracellular action potentials.

#### 297 4. Intra-cortical extracellular potentials from neural populations

298 Extracellular potentials measured within neural tissue are often split into two separate frequency  
 299 domains, which reflect different aspects of the underlying neural activity. The low frequency part, that  
 300 is, the local field potential (LFP), is thought to mostly reflect synaptic input to populations of pyramidal  
 301 cells, while the high-frequency part, that is, the multi-unit activity (MUA), reflects the population  
 302 spiking activity (Fig. 4).



**Figure 4: Extracellular potentials from different waves of synaptic input.** Different brain signals from separate waves of synaptic input to 10 000 layer 5 pyramidal cells from rat [Hay et al., 2011]. **A:** A subset of 100 pyramidal cells, with the LFP electrode locations indicated in the center (colored dots). **B:** Depth-resolved synaptic inputs arrive in three waves, first targeting the basal dendrites ( $t=100$  ms), then the apical dendrites ( $t=200$  ms), and lastly uniformly across the entire depth ( $t=300$  ms). Note that all synaptic input is pre-defined, that is, there is no network activity. **C:** The extracellular potential at different depths (corresponding to dots in panel A), including both spikes and synaptic input. **D:** The LFP, that is, a low-pass filtered version of the raw signal in C. **E:** The MUA, that is, a high-pass filtered version of the raw signal in C. **F:** Another version of the MUA which is a rectified and low-pass filtered version of the MUA signal in E. All filters were 4th order Butterworth filters in forward-backward mode [NeuroEnsemble, 2017]. For illustration purposes a relatively low cut-off frequency of 50 Hz was chosen for the LFP low-pass filter. The MUA was first high-pass filtered above 300 Hz (E and F), then rectified and low-pass filtered below 300 Hz (F).

#### 303 4.1. Local field potentials

304 The LFP is the low-frequency part ( $\lesssim 500$  Hz) of the extracellular potentials, and it is among the  
 305 oldest and most used brain signals in neuroscience [Einevoll et al., 2013a]. The LFP is expected  
 306 to be dominated by synaptic inputs asymmetrically placed onto populations of geometrically aligned  
 307 neurons [Nunez and Srinivasan, 2006; Lindén et al., 2011; Einevoll et al., 2013b]. In cortex and  
 308 hippocampus, neurons can broadly speaking be divided into two main classes: the inhibitory in-  
 309 terneurons, and the excitatory pyramidal neurons. Pyramidal neurons typically have a clear axis of  
 310 orientation, that is, the apical dendrites of close-by pyramidal neurons tend to be oriented in the same  
 311 direction (Fig. 4A). This geometrical alignment is important because the LFP contributions from the  
 312 individual pyramidal cells also align and therefore sum constructively. For example, basal excita-  
 313 tory synaptic input (Fig. 4B, time marked by red line) generates a current sink and correspondingly  
 314 negative LFP deflection in the basal region, and simultaneously a current source and correspondingly  
 315 positive LFP deflection in the apical region (Fig. 4D, time marked by red line), while apical excita-  
 316 tory synaptic input leads to the reversed pattern (Fig. 4B,D, time marked by blue line). Importantly,

317 this means that excitatory input that simultaneously targets both the apical and the basal dendrite  
318 will give opposite source/sink patterns which will lead to substantial cancellation and a weak LFP  
319 contribution (Fig. 4B, D, time marked by orange line). The same arguments also apply to inhibitory  
320 synaptic inputs, with the signs of the currents and LFPs reversed.

321 Note that, for example, the LFP signature of apical excitatory synaptic input is inherently similar  
322 to that of basal inhibitory input, and indeed, separating between cases like this pose a real challenge  
323 in interpreting LFP signals [Lindén et al., 2010].

324 In contrast to pyramidal neurons, interneurons often lack any clear orientational specificity, meaning  
325 that the current dipoles from individual interneurons, which might by themselves be sizable  
326 [Lindén et al., 2010], do not align, leading to negligible net contributions to LFP signals [Mazzoni  
327 et al., 2015]. Note, however, that the interneurons may indirectly cause large LFP contributions  
328 through their synaptic inputs onto pyramidal cells [Teleńczuk et al., 2017; Hagen et al., 2016].

329 It has been demonstrated that correlations among the synaptic inputs to pyramidal cells can  
330 amplify the LFP signal power by orders of magnitude, with the implication that populations receiving  
331 correlated synaptic input can dominate the LFP also 1-2 mm outside of the population [Lindén et al.,  
332 2011; Łęski et al., 2013].

333 Somatic action potentials lasting only a few milliseconds are generally expected to contribute little  
334 to cortical LFP signals [Pettersen et al., 2008; Pettersen and Einevoll, 2008; Einevoll et al., 2013a;  
335 Haider et al., 2016]: Their very short duration with both positive and negative phases (Fig. 3E)  
336 will typically give large signal cancellations of the contributions from individual neurons, and their  
337 high frequency content is to a large degree removed from LFPs during low-pass filtering. Note,  
338 however, that in the hippocampus the highly synchronized spikes found during sharp wave ripples  
339 are expected to also contribute to shaping of the LFP [Schomburg et al., 2012; Luo et al., 2018].

340 Other active conductances may contribute in shaping the LFP, for example, the slower dendritic  
341 calcium spikes [Suzuki and Larkum, 2017] or long-lasting after-hyperpolarization currents [Reimann  
342 et al., 2013]. Further, subthreshold active conductances can also shape the LFP by molding the  
343 transmembrane currents following synaptic input, and the hyperpolarization-activated cation channel  
344  $I_h$  may play a key role in this, both through asymmetrically changing the membrane conductance,  
345 and by introducing apparent resonance peaks in the LFP [Ness et al., 2016, 2018].

#### 346 4.2. MUA

347 While LFPs are thought to mainly reflect the synaptic input to large populations of pyramidal neu-  
348 rons, the multi-unit activity (MUA) can be used to probe the population spiking activity [Einevoll et al.,  
349 2007; Pettersen et al., 2008] (Fig. 4 E,F). In other words, the MUA holds complimentary information  
350 to the LFP. In particular, this can be useful for some cell-types, like stellate cells and **inhibitory**  
351 interneurons, which are expected to have very weak LFP contributions [Lindén et al., 2011], but might  
352 still be measurable through their spiking activity. Similarly, spatially uniformly distributed synaptic  
353 input to pyramidal neurons results in a negligible LFP contribution (Fig. 4C, time marked by orange  
354 line), while the population might still contribute substantially to the MUA through the extracellular  
355 action potentials (Fig. 4E-F, time marked by orange line).

356 **5. ECoG and EEG**

357 In order to measure electric potentials in the immediate vicinity of neurons, like LFP and MUA  
 358 signals, we need to insert sharp electrodes into the brain. This highly invasive technique is quite  
 359 common in animal studies, but can only be applied to humans when there is a clear medical need, for  
 360 example in patients with intractable epilepsy [Zangibadi et al., 2019]. However, electric potentials  
 361 generated by neural activity extend beyond neural tissue and can also be measured outside the  
 362 brain: Placing electrodes on the brain surface, as in electrocorticography (ECoG), is a technique  
 363 that requires some surgery. With electroencephalography (EEG), on the other hand, potentials are  
 364 measured non-invasively, directly on top of the scalp.

365 Since EEG electrodes are located relatively far away from the neuronal sources, the current  
 366 dipole approximation, eq. (12), combined with some head model, can be applied for computing EEG  
 367 signals [Nunez and Srinivasan, 2006; Ilmoniemi and Sarvas, 2019]. By collapsing the transmem-  
 368 brane currents of a neuron simulation into one single current dipole moment, see eq. (13), we can  
 369 calculate EEG from arbitrary neural activity (Fig. 5). The current dipole approximation is however  
 370 not unproblematic to use for computing ECoG signals, as the ECoG electrodes may be located too  
 371 close to the signal sources for the approximation to apply, see Hagen et al. [2018].

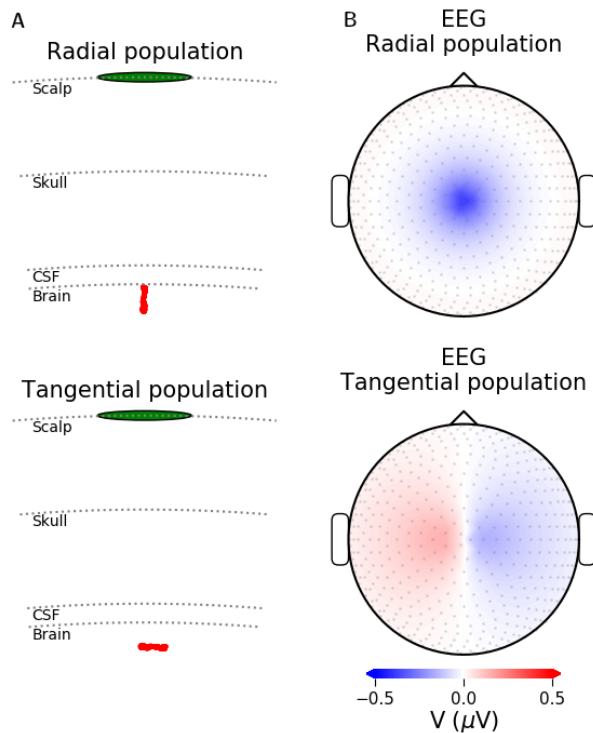


Figure 5: **EEG from apical synaptic input to population of pyramidal cells.** **A:** The four-sphere head model with two orientations of the neural population from Fig. 4, either radial, mimicking a population in a gyrus (top) or tangential, mimicking a population in a sulcus (bottom). **B:** A snapshot of the EEG signal at the head surface for apical input (time marked with blue dotted line in Fig. 4), for a radial population (top) or tangential population (bottom).

372    5.1. Head models

373    Electric potentials measured on the scalp surface will be affected by the geometries and con-  
 374    ductivities of the different constituents of the head [Nunez and Srinivasan, 2006]. This can be in-  
 375    corporated in EEG calculations by applying simplified or more complex head models. A well-known  
 376    simplified head model is the analytical four-sphere model, consisting of four concentric shells rep-  
 377    resenting brain tissue, cerebrospinal fluid (CSF), skull and scalp, where the conductivity can be set  
 378    individually for each shell [Næss et al., 2017; Srinivasan et al., 1998; Nunez and Srinivasan, 2006]  
 379    (Fig. 6, Fig. 7A,B). More complex head models make use of high-resolution anatomical MRI-data  
 380    to map out a geometrically detailed head volume conductor. The link between current dipoles in  
 381    the brain and resulting EEG signals is determined applying numerical methods such as the finite  
 382    element method [Larson and Bengzon, 2013; Logg et al., 2012]. Once this link is established we  
 383    can in principle insert a dipole representing arbitrary neural activity into such a model, and compute  
 384    the resulting EEG signals quite straightforwardly. The New York Head model is an example of one  
 385    such pre-solved complex head model, see Fig. 7C,D [Huang et al., 2016].

386    The head models themselves introduce no essential frequency filtering of the EEG signal [Pfurtscheller  
 387    and Cooper, 1975; Nunez and Srinivasan, 2006; Ranta et al., 2017], however, substantial spatial fil-  
 388    tering will occur (Fig. 6). Additionally, the measured (or modeled) signals represent the average  
 389    potential across the electrode surface, and the large electrode sizes used in ECoG/EEG recordings  
 390    can have important effect on the measured signals [Nunez and Srinivasan, 2006; Hagen et al., 2018;  
 391    Dubey and Ray, 2019].

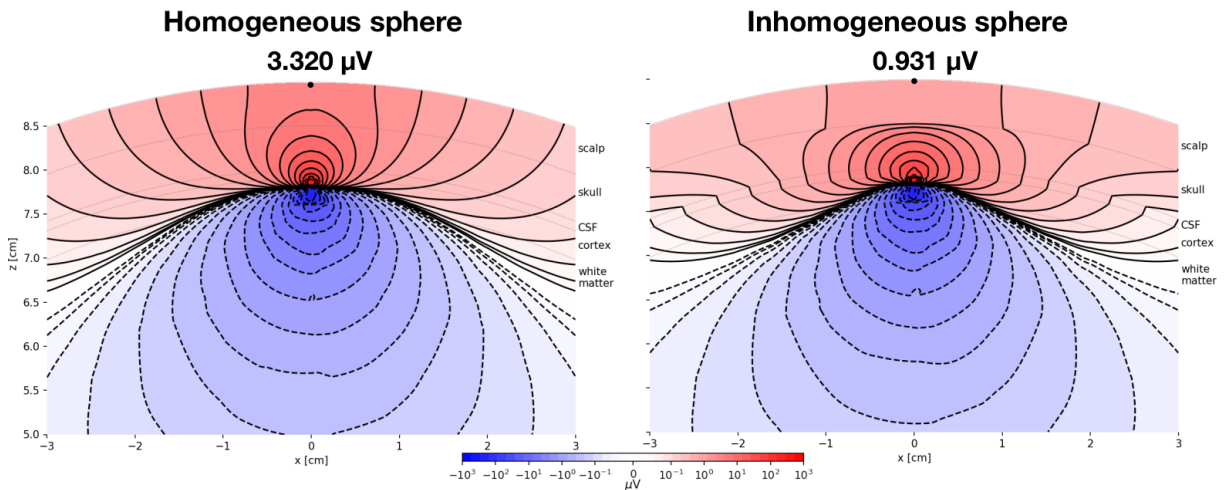


Figure 6: **Effect of head inhomogeneities.** The same current dipole will give substantially different potentials on the head surface if the different conductivities of the head is included in a FEM model [Næss et al., 2017]. Left: Homogeneous sphere, with electrical conductivity,  $\sigma = 0.33 \text{ S/m}$  everywhere. Right: Standard four-sphere head model, with  $\sigma_{\text{brain}} = 0.33 \text{ S/m}$ ,  $\sigma_{\text{CSF}} = 5\sigma_{\text{brain}}$ ,  $\sigma_{\text{skull}} = \sigma_{\text{brain}}/20$ ,  $\sigma_{\text{scalp}} = \sigma_{\text{brain}}$ .

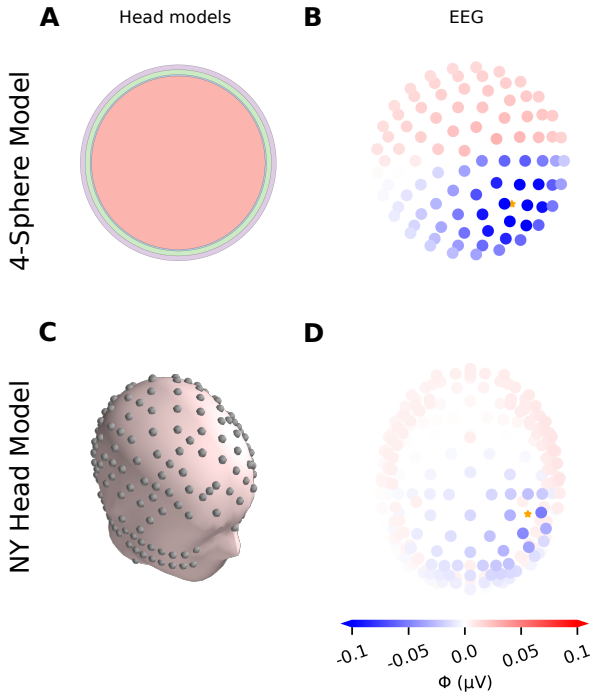


Figure 7: **The four-sphere head model and the NY Head model.** EEG signals from population dipole resulting from waves of synaptic input to 10 000 layer 5 pyramidal cells from rat [Hay et al., 2011]. **A:** The four-sphere model consisting of four concentrical shells: brain, CSF, skull and scalp. **B:** Maximum EEG signals ( $\phi$ ) on scalp surface electrodes resulting from population dipole placed at location marked by orange star, computed with the four-sphere model. **C:** Illustration of the New York Head model. **D:** EEG signals computed with the New York Head model, equivalent to panel **B**.

## 392 6. Discussion

393 In the present chapter we have derived and applied well-established biophysical forward-modeling  
 394 schemes for computing extracellular electrical potentials recorded inside and outside the brain.  
 395 These electrical potentials include spikes (both single-unit and multiunit activity (MUA)), LFP, ECoG  
 396 and EEG signals. The obvious application of this scheme is computation of electrical signals from  
 397 neuron and network activity for comparison with experiments so that candidate models can be  
 398 tested [Einevoll et al., 2019] or inferred [Goncalves et al., 2019; Skaar et al., 2020]. Another key  
 399 application is the computation of benchmarking data for testing of data analysis methods such as  
 400 spike sorting or CSD analysis [Denker et al., 2012].

401 Inverse modeling of recorded electrical potentials, that is, estimation of the neural sources un-  
 402 derlying the signals, is inherently an ill-posed problem. This means that no unique solution for the

403 size and position of the sources exists. However, prior knowledge about the underlying sources and  
404 how they generate the recorded signals, can be used to increase the identifiability. For example,  
405 several methods for the estimation of so-called current-source density (CSD) from LFP recordings  
406 have been developed by building the present forward model into the CSD estimator [Pettersen et al.,  
407 2006; Potworowski et al., 2012; Cserpán et al., 2017].

408 The present chapter has focused on the modeling of measurements of extracellular electrical  
409 signals. Another important and related brain signal is the magnetic fields recorded outside the head  
410 in magnetoencephalography (MEG). These magnetic signals also stem from the transmembrane cur-  
411 rents of neurons and, similar to EEG, the signal can be computed based on the current dipoles of  
412 the underlying neurons in cortex [Hämäläinen et al., 1993; Ilmoniemi and Sarvas, 2019]. The new  
413 version of our tool LFPy, which was used in generating the examples in the present chapter, thus  
414 also includes the ability to compute MEG signals [Hagen et al., 2018].

415 There are also other measurement modalities where detailed modeling could be pursued to al-  
416 low for a more quantitative analysis of recorded data. Voltage-sensitive dye imaging (VSDI) reflects  
417 area-weighted neuronal membrane potentials [Chemla and Chavane, 2012], while two-photon cal-  
418 cium imaging measures the intracellular calcium dynamics [Helmchen, 2012]. Both are accessible  
419 through neuronal simulations of the type used to compute electrical and magnetic signals. Func-  
420 tional magnetic resonance imaging (fMRI) instead reflect blood dynamics [Bartels et al., 2012], which  
421 typically are not explicitly included in neural network models.

## 422 Acknowledgements

423 This research has received funding from the European Union Horizon 2020 Framework Pro-  
424 gramme for Research and Innovation under Specific Grant Agreement No. 785907 (Human Brain  
425 Project SGA2), and the Research Council of Norway (Notur, nn4661k; DigiBrain, no. 248828; INCF  
426 National Node, no. 269774).

427 Almeida, A. C. G., Texeira, H. Z., Duarte, M. A., Infantosi, A. F. C., March 2004. Modeling extra-  
428 cellular space electrodiffusion during lea/spl tilde/o's spreading depression. IEEE Transactions on  
429 Biomedical Engineering 51 (3), 450–458.

430 Bartels, A., Goense, J., Logothetis, N., Sep. 2012. Functional magnetic resonance imaging. In:  
431 Brette, R., Destexhe, A. (Eds.), Handbook of Neural Activity Measurement. Cambridge University  
432 Press, pp. 92–135.

433 Billeh, Y. N., Cai, B., Gratiy, S. L., Dai, K., Iyer, R., Gouwens, N. W., Abbasi-Asl, R., Jia, X., Siegle,  
434 J. H., Olsen, S. R., Koch, C., Mihalas, S., Arkhipov, A., 2020. Systematic integration of structural  
435 and functional data into multi-scale models of mouse primary visual cortex. Neuron.  
436 URL <https://www.biorxiv.org/content/early/2019/06/06/662189>

437 Buccino, A. P., Einevoll, G. T., 2019. Mearec: a fast and customizable testbench simulator for ground-  
438 truth extracellular spiking activity. bioRxiv.  
439 URL <https://www.biorxiv.org/content/early/2019/07/03/691642>

440 Buccino, A. P., Kordovan, M., Ness, T. V., Merkt, B., Häfliger, P. D., Fyhn, M., Cauwenberghs, G., Rot-  
441 ter, S., Einevoll, G. T., 2018. Combining biophysical modeling and deep learning for multi-electrode

- 442 array neuron localization and classification. *Journal of Neurophysiology* 120, 1212–1232.  
443 URL <http://www.ncbi.nlm.nih.gov/pubmed/29847231><https://www.physiology.org/doi/10.1152/jn.00210.2018>
- 445 Buccino, A. P., Kuchta, M., Jæger, K. H., Ness, T. V., Berthet, P., Mardal, K.-A., Cauwenberghs, G.,  
446 Tveito, A., 2019. How does the presence of neural probes affect extracellular potentials? *Journal  
447 of Neural Engineering* 16 (2).
- 448 Buzsáki, G., Anastassiou, C. a., Koch, C., Jun. 2012. The origin of extracellular fields and currents—  
449 EEG, ECoG, LFP and spikes. *Nature reviews. Neuroscience* 13 (6), 407–20.  
450 URL <http://www.ncbi.nlm.nih.gov/pubmed/22595786>
- 451 Chemla, S., Chavane, F., Sep. 2012. Voltage-sensitive dye imaging. In: Brette, R., Destexhe, A.  
452 (Eds.), *Handbook of Neural Activity Measurement*. Cambridge University Press, pp. 92–135.
- 453 Cserpán, D., Meszéna, D., Wittner, L., Tóth, K., Ulbert, I., Somogyvári, Z., Wójcik, D. K., Nov. 2017.  
454 Revealing the distribution of transmembrane currents along the dendritic tree of a neuron from  
455 extracellular recordings. *eLife* 6.
- 456 Delgado Ruz, I., Schultz, S. R., 2014. Localising and classifying neurons from high density MEA  
457 recordings. *Journal of Neuroscience Methods* 233, 115–128.  
458 URL <http://dx.doi.org/10.1016/j.jneumeth.2014.05.037>
- 459 Denker, M., Einevoll, G., Franke, F., Grün, S., Hagen, E., Kerr, J., Nawrot, M., Ness, T. B., Wójcik,  
460 T. W. D., 2012. Report from 1st incf workshop on validation of analysis methods. Tech. rep.,  
461 International Neuroinformatics Coordinating Facility (INCF).
- 462 Dubey, A., Ray, S., 2019. Cortical electrocorticogram (ecog) is a local signal. *Journal of Neuro-  
463 science* 39 (22), 4299–4311.
- 464 Einevoll, G., Kayser, C., Logothetis, N., Panzeri, S., 2013a. Modelling and analysis of local field  
465 potentials for studying the function of cortical circuits. *Nature Reviews Neuroscience* 14, 770–  
466 785.
- 467 Einevoll, G. T., Destexhe, A., Diesmann, M., Grün, S., Jirsa, V., de Kamps, M., Migliore, M., Ness,  
468 T. V., Plesser, H. E., Schürmann, F., 2019. The Scientific Case for Brain Simulations. *Neuron*  
469 102 (4), 735–744.
- 470 Einevoll, G. T., Lindén, H., Tetzlaff, T., Łęski, S., Pettersen, K. H., 2013b. Local Field Potentials  
471 - Biophysical Origin and Analysis. In: Quiroga, R. Q., Panzeri, S. (Eds.), *Principles of Neural  
472 Coding*. CRC Press, Boca Raton, FL, Ch. 3, pp. 37–60.
- 473 Einevoll, G. T., Pettersen, K. H., Devor, A., Ulbert, I., Halgren, E., Dale, A. M., Mar. 2007. Lami-  
474 nar population analysis: estimating firing rates and evoked synaptic activity from multielectrode  
475 recordings in rat barrel cortex. *Journal of neurophysiology* 97 (3), 2174–90.  
476 URL <http://www.ncbi.nlm.nih.gov/pubmed/17182911>
- 477 Elbohouty, M., 2013. Electrical Conductivity of Brain Cortex Slices in Seizing and Non-seizing States.  
478 Ph.D. thesis, The University of Waikato.

- 479 Ellingsrud, A. J., Solbrå, A., Einevoll, G. T., Halnes, G., Rognes, M. E., 2020. Finite element simulation  
480 of ionic electrodiffusion in cellular geometries. *Frontiers in Neuroinformatics* 14, 11.  
481 URL <https://www.frontiersin.org/article/10.3389/fninf.2020.00011>
- 482 Frey, U., Egert, U., Heer, F., Hafizovic, S., Hierlemann, a., mar 2009. Microelectronic system for  
483 high-resolution mapping of extracellular electric fields applied to brain slices. *Biosensors & bio-*  
484 *electronics* 24 (7), 2191–8.  
485 URL <http://www.ncbi.nlm.nih.gov/pubmed/19157842>
- 486 Gabriel, S., Lau, R. W., Gabriel, C., nov 1996. The dielectric properties of biological tissues: II.  
487 Measurements in the frequency range 10 Hz to 20 GHz. *Physics in medicine and biology* 41 (11),  
488 2251–69.  
489 URL <http://www.ncbi.nlm.nih.gov/pubmed/8938025>
- 490 Gardner, C. L., Jones, J. R., Baer, S. M., Crook, S. M., Feb. 2015. Drift-diffusion simulation of the  
491 ephaptic effect in the triad synapse of the retina. *Journal of computational neuroscience* 38 (1),  
492 129–42.  
493 URL <http://www.ncbi.nlm.nih.gov/pubmed/25260382>
- 494 Gold, C., Henze, D. A., Koch, C., Aug 2007. Using extracellular action potential recordings to con-  
495 strain compartmental models. *J. Comput. Neurosci.* 23 (1), 39–58.  
496 URL <http://dx.doi.org/10.1007/s10827-006-0018-2>
- 497 Goncalves, P. J., Lueckmann, J.-M., Deistler, M., Nonnenmacher, M., Öcal, K., Bassetto, G., Chin-  
498 taluri, C., Podlaski, W. F., Haddad, S. A., Vogels, T. P., Greenberg, D. S., Macke, J. H., 2019. Training  
499 deep neural density estimators to identify mechanistic models of neural dynamics. *bioRxiv*.
- 500 Goto, T., Hatanaka, R., Ogawa, T., Sumiyoshi, A., Riera, J., Kawashima, R., 2010. An evaluation of  
501 the conductivity profile in the somatosensory barrel cortex of wistar rats. *Journal of neurophysiology* 104 (6), 3388–3412.
- 503 Gratiy, S. L., Halnes, G., Denman, D., Hawrylycz, M. J., Koch, C., Einevoll, G. T., Anastassiou,  
504 C. A., 2017. From Maxwell's equations to the theory of current-source density analysis. *European*  
505 *Journal of Neuroscience* 45 (8), 1013–1023.
- 506 Grodzinsky, F., 2011. *Fields, Forces, and Flows in Biological Systems*. Garland Science, Taylor &  
507 Francis Group, London & New York.
- 508 Głabska, H., Potworowski, J., Łęski, S., Wójcik, D. K., 2014. Independent components of neural  
509 activity carry information on individual populations. *PLoS One* 9 (8), e105071.  
510 URL <http://dx.doi.org/10.1371/journal.pone.0105071>
- 511 Głabska, H. T., Norheim, E., Devor, A., Dale, A. M., Einevoll, G. T., Wójcik, D. K., 2016. Generalized  
512 laminar population analysis (glpa) for interpretation of multielectrode data from cortex. *Frontiers*  
513 *in neuroinformatics* 10, 1.
- 514 Hagen, E., Dahmen, D., Stavrinou, M. L., Lindén, H., Tetzlaff, T., Van Albada, S. J., Grün, S.,  
515 Diesmann, M., Einevoll, G. T., 2016. Hybrid scheme for modeling local field potentials from point-  
516 neuron networks. *Cerebral Cortex* 26 (12), 4461–4496.

- 517 Hagen, E., Næss, S., Ness, T. V., Einevoll, G. T., 2018. Multimodal modeling of neural network  
518 activity: computing LFP, ECoG, EEG and MEG signals with LFPy 2.0. *Front Neuroinform* 12 (92).
- 519 Hagen, E., Næss, S., Ness, T. V., Einevoll, G. T., 2019. LFPy – multimodal modeling of extracellular  
520 neuronal recordings in Python. In: *Encyclopedia of Computational Neuroscience*. Springer, New  
521 York, NY, p. 620286.
- 522 URL <http://biorxiv.org/content/early/2019/05/03/620286.abstract>
- 523 Haider, B., Schulz, D. P. A., Häusser, M., Carandini, M., 2016. Millisecond Coupling of Local Field  
524 Potentials to Synaptic Currents in the Awake Visual Cortex. *Neuron* 90, 35–42.
- 525 Halnes, G., Mäki-Marttunen, T., Keller, D., Pettersen, K. H., Andreassen, O. A., Einevoll, G. T., 2016.  
526 Effect of ionic diffusion on extracellular potentials in neural tissue. *PLoS computational biology*  
527 12 (11), e1005193.
- 528 Halnes, G., Mäki-Marttunen, T., Pettersen, K. H., Andreassen, O. A., Einevoll, G. T., 2017. Ion diffu-  
529 sion may introduce spurious current sources in current-source density (CSD) analysis. *Journal of*  
530 *Neurophysiology* 118 (1), 114–120.
- 531 URL <http://jn.physiology.org/lookup/doi/10.1152/jn.00976.2016>
- 532 Halnes, G., Østby, I., Pettersen, K. H., Omholt, S. W., Einevoll, G. T., 2015. An Electrodiffusive For-  
533 malism for Ion Concentration Dynamics in Excitable Cells and the Extracellular Space Surrounding  
534 Them. In: *Advances in cognitive neurodynamics (IV)*. Springer Netherlands, pp. 353–360.
- 535 URL [http://link.springer.com/chapter/10.1007/978-94-017-9548-7\\_50](http://link.springer.com/chapter/10.1007/978-94-017-9548-7_50)
- 536 Halnes, G., Østby, I., Pettersen, K. H., Omholt, S. W., Einevoll, G. T., 2013. Electrodiffusive model  
537 for astrocytic and neuronal ion concentration dynamics. *PLoS computational biology* 9 (12),  
538 e1003386.
- 539 Hämäläinen, M., Hari, R., Ilmoniemi, R. J., Knuutila, J., Lounasmaa, O. V., 1993. Magnetoen-  
540 cephalography?theory, instrumentation, and applications to noninvasive studies of the working  
541 human brain. *Reviews of modern Physics* 65 (2), 413.
- 542 Haufe, S., Huang, Y., Parra, L. C., 2015. A highly detailed FEM volume conductor model based on  
543 the ICBM152 average head template for EEG source imaging and TCS targeting. Conference pro-  
544 ceedings : ... Annual International Conference of the IEEE Engineering in Medicine and Biology  
545 Society. IEEE Engineering in Medicine and Biology Society. Annual Conference 2015, 5744–5747.
- 546 Hay, E., Hill, S., Schürmann, F., Markram, H., Segev, I., jul 2011. Models of neocortical layer 5b  
547 pyramidal cells capturing a wide range of dendritic and perisomatic active properties. *PLoS*  
548 *Computational Biology* 7 (7), 1–18.
- 549 URL <http://www.ncbi.nlm.nih.gov/pmc/articles/PMC3145650/>{&}tool=pmcentrez{&}rendertype=abstract
- 550
- 551 Helmchen, F., Sep. 2012. Calcium imaging. In: Brette, R., Destexhe, A. (Eds.), *Handbook of Neural*  
552 *Activity Measurement*. Cambridge University Press, pp. 92–135.

- 553 Holsheimer, J., 1987. Electrical conductivity of the hippocampal ca1 layers and application to current-  
554 source-density analysis. *Experimental brain research* 67 (2), 402–410.
- 555 Holt, G., Koch, C., 1999. Electrical interactions via the extracellular potential near cell bodies. *Journal*  
556 *of computational neuroscience* 6, 169–184.  
557 URL <http://link.springer.com/article/10.1023/A:1008832702585>
- 558 Huang, Y., Parra, L. C., Haufe, S., 2016. The New York Head—A precise standardized volume  
559 conductor model for EEG source localization and tES targeting. *NeuroImage* 140, 150–162.  
560 URL <http://dx.doi.org/10.1016/j.neuroimage.2015.12.019>
- 561 Ilmoniemi, R. J., Sarvas, J., 2019. Brain Signals - Physics and Mathematics of MEG and EEG. MIT  
562 Press, Cambridge, Massachusetts; London, England.
- 563 Jackson, J. D., 1998. Classical electrodynamics, 3rd Edition. Wiley.
- 564 Joucla, S., Yvert, B., 2012. Modeling extracellular electrical neural stimulation: from basic under-  
565 standing to MEA-based applications. *Journal of physiology, Paris* 106 (3-4), 146–58.  
566 URL <http://www.ncbi.nlm.nih.gov/pubmed/22036892>
- 567 Koch, C., 1999. Biophysics of computation: information processing in single neurons., 1st Edition.  
568 Oxford University Press: New York.
- 569 Larson, M. G., Bengzon, F., 2013. The finite element method: theory, implementation, and applica-  
570 tions. Vol. 10. Springer Science & Business Media.
- 571 Łęski, S., Pettersen, K. H., Tunstall, B., Einevoll, G. T., Gigg, J., Wójcik, D. K., Dec. 2011. Inverse  
572 current source density method in two dimensions: inferring neural activation from multielectrode  
573 recordings. *Neuroinformatics* 9 (4), 401–25.  
574 URL <http://www.ncbi.nlm.nih.gov/entrez/query.fcgi?artid=3214268&tool=pmcentrez&rendertype=abstract>
- 576 Léonetti, M., Dubois-Violette, E., Aug. 1998. Theory of Electrodynamic Instabilities in Biological  
577 Cells. *Physical Review Letters* 81 (9), 1977–1980.  
578 URL <http://link.aps.org/doi/10.1103/PhysRevLett.81.1977>
- 579 Léonetti, M., Dubois-Violette, E., Homblé, F., Jul. 2004. Pattern formation of stationary transcellular  
580 ionic currents in Fucus. *Proceedings of the National Academy of Sciences of the United States of*  
581 *America* 101 (28), 10243–8.  
582 URL <http://www.ncbi.nlm.nih.gov/entrez/query.fcgi?artid=478558&tool=pmcentrez&rendertype=abstract>
- 584 Łęski, S., Lindén, H., Tetzlaff, T., Pettersen, K. H., Einevoll, G. T., 2013. Frequency dependence of  
585 signal power and spatial reach of the local field potential. *PLoS Comput Biol* 9 (7), e1003137.
- 586 Lindén, H., Hagen, E., Łęski, S., Norheim, E. S., Pettersen, K. H., Einevoll, G. T., jan 2014. LFPy:  
587 a tool for biophysical simulation of extracellular potentials generated by detailed model neurons.  
588 *Frontiers in Neuroinformatics* 7 (41), 1–15.  
589 URL <http://journal.frontiersin.org/article/10.3389/fninf.2013.00041/abstract>

- 590 Lindén, H., Pettersen, K. H., Einevoll, G. T., dec 2010. Intrinsic dendritic filtering gives low-pass  
591 power spectra of local field potentials. *Journal of computational neuroscience* 29 (3), 423–44.  
592 URL <http://www.ncbi.nlm.nih.gov/pubmed/20502952>
- 593 Lindén, H., Tetzlaff, T., Potjans, T. C., Pettersen, K. H., Grün, S., Diesmann, M., Einevoll, G. T., Dec.  
594 2011. Modeling the spatial reach of the LFP. *Neuron* 72 (5), 859–72.  
595 URL <http://www.ncbi.nlm.nih.gov/pubmed/22153380>
- 596 Logg, A., Mardal, K.-A., Wells, G., 2012. Automated solution of differential equations by the finite  
597 element method: The FEniCS book. Vol. 84. Springer Science & Business Media, Berlin, Heidelberg.
- 598 Logothetis, N. K., Kayser, C., Oeltermann, A., sep 2007. In vivo measurement of cortical impedance  
599 spectrum in monkeys: implications for signal propagation. *Neuron* 55 (5), 809–23.  
600 URL <http://www.ncbi.nlm.nih.gov/pubmed/17785187>
- 602 López-Aguado, L., Ibarz, J., Herreras, O., 2001. Activity-dependent changes of tissue resistivity in  
603 the ca1 region in vivo are layer-specific: modulation of evoked potentials. *Neuroscience* 108 (2),  
604 249–262.
- 605 Lopreore, C. L., Bartol, T. M., Coggan, J. S., Keller, D. X., Sosinsky, G. E., Ellisman, M. H.,  
606 Sejnowski, T. J., Sep. 2008. Computational modeling of three-dimensional electrodiffusion in  
607 biological systems: application to the node of Ranvier. *Biophysical journal* 95 (6), 2624–35.  
608 URL <http://www.ncbi.nlm.nih.gov/pmc/articles/PMC2527256/>&tool=pmcentrez&rendertype=abstract
- 610 Lu, B., Zhou, Y. C., Huber, G. a., Bond, S. D., Holst, M. J., McCammon, J. A., Oct. 2007. Electrod-  
611 iffusion: a continuum modeling framework for biomolecular systems with realistic spatiotemporal  
612 resolution. *The Journal of chemical physics* 127 (13), 135102.  
613 URL <http://www.ncbi.nlm.nih.gov/pubmed/17919055>
- 614 Luo, J., Macias, S., Ness, T. V., Einevoll, G. T., Zhang, K., Moss, C. F., 2018. Neural timing of stimulus  
615 events with microsecond precision. *PLoS biology* 16 (10), 1–22.
- 616 Markram, H., Muller, E., Ramaswamy, S., Reimann, M. W., Abdellah, M., Sanchez, C. A., Ailamaki,  
617 A., Alonso-Nanclares, L., Antille, N., Arsever, S., et al., 2015. Reconstruction and simulation of  
618 neocortical microcircuitry. *Cell* 163 (2), 456–492.
- 619 Martinsen, Ø. G., Grimnes, S., 2008. Bioimpedance and Bioelectricity Basics. Academic Press; 2  
620 edition.  
621 URL <http://www.amazon.com/Bioimpedance-Bioelectricity-Basics-Second-Edition/dp/0123740045>
- 623 Mazzoni, A., Lindén, H., Cuntz, H., Lansner, A., Panzeri, S., Einevoll, G. T., 2015. Computing  
624 the local field potential (lfp) from integrate-and-fire network models. *PLoS Comput Biol* 11 (12),  
625 e1004584.

- 626 McIntyre, C. C., Grill, W. M., Mar. 2001. Finite Element Analysis of the Current-Density and Electric  
627 Field Generated by Metal Microelectrodes. *Annals of Biomedical Engineering* 29 (3), 227–235.  
628 URL <http://www.springerlink.com/openurl.asp?id=doi:10.1114/1.1352640>
- 629 Mechler, F., Victor, J. D., Jun. 2012. Dipole characterization of single neurons from their extracellular  
630 action potentials. *Journal of computational neuroscience* 32(1), 73–100.  
631 URL <http://www.ncbi.nlm.nih.gov/pubmed/21667156>
- 632 Miceli, S., Ness, T. V., Einevoll, G. T., Schubert, D., 2017. Impedance spectrum in cortical tissue:  
633 Implications for propagation of Ifp signals on the microscopic level. *eNeuro* 4 (1).  
634 URL <https://www.eneuro.org/content/4/1/ENEURO.0291-16.2016>
- 635 Mitzdorf, U., 1985. Current source-density method and application in cat cerebral cortex: investigation  
636 of evoked potentials and eeg phenomena. *Physiological reviews* 65 (1), 37–100.
- 637 Moffitt, M. a., McIntyre, C. C., sep 2005. Model-based analysis of cortical recording with silicon  
638 microelectrodes. *Clinical neurophysiology* 116 (9), 2240–50.  
639 URL <http://www.ncbi.nlm.nih.gov/pubmed/16055377>
- 640 Mori, Y., 2009. From three-dimensional electrophysiology to the cable model: an asymptotic study.  
641 arXiv preprint arXiv:0901.3914, 1–39.  
642 URL <http://arxiv.org/abs/0901.3914>
- 643 Mori, Y., Fishman, G. I., Peskin, C. S., Apr. 2008. Ephaptic conduction in a cardiac strand model  
644 with 3D electrodiffusion. *Proceedings of the National Academy of Sciences of the United States  
645 of America* 105 (17), 6463–8.  
646 URL <http://www.pubmedcentral.nih.gov/articlerender.fcgi?artid=2359793&tool=pmcentrez&rendertype=abstract>
- 648 Mori, Y., Liu, C., Eisenberg, R. S., 2011. A Model of Electrodiffusion and Osmotic Water Flow and  
649 its Energetic Structure. arXiv preprint arXiv:1101.5193.
- 650 Mori, Y., Peskin, C., 2009. A numerical method for cellular electrophysiology based on the electrod-  
651 iffusion equations with internal boundary conditions at membranes. *Communications in Applied  
652 Mathematics and Computational Science* 4.1, 85–134.  
653 URL <http://msp.org/camcos/2009/4-1/p04.xhtml>
- 654 Moulin, C., Glière, A., Barbier, D., Joucla, S., Yvert, B., Mailley, P., Guillemaud, R., Feb. 2008. A new  
655 3-D finite-element model based on thin-film approximation for microelectrode array recording of  
656 extracellular action potential. *IEEE transactions on bio-medical engineering* 55 (2 Pt 1), 683–92.  
657 URL <http://www.ncbi.nlm.nih.gov/pubmed/18270005>
- 658 Næss, S., Chintaluri, C., Ness, T. V., Dale, A. M., Einevoll, G. T., Wójcik, D. K., 2017. Corrected  
659 Four-Sphere Head Model for EEG Signals. *Frontiers in Human Neuroscience* 11 (October), 1–7.  
660 URL <http://journal.frontiersin.org/article/10.3389/fnhum.2017.00490/full>
- 661 Nanninga, P., 2008. A computational neuron model based on Poisson-Nernst-Planck theory.  
662 ANZIAM Journal 50, 46–59.  
663 URL <http://journal.austms.org.au/ojs/index.php/anziamj/article/view/1390>

- 664 Nelson, M. J., Pouget, P., may 2010. Do electrode properties create a problem in interpreting local  
665 field potential recordings? *Journal of neurophysiology* 103 (5), 2315–7.  
666 URL <http://www.ncbi.nlm.nih.gov/pubmed/20220081>
- 667 Ness, T. V., Chintaluri, C., Potworowski, J., Łęski, S., Głabska, H., Wójcik, D. K., Einevoll, G. T.,  
668 2015. Modelling and Analysis of Electrical Potentials Recorded in Microelectrode Arrays (MEAs).  
669 *Neuroinformatics* 13 (4), 403–426.  
670 URL <http://link.springer.com/10.1007/s12021-015-9265-6>
- 671 Ness, T. V., Remme, M. W. H., Einevoll, G. T., 2016. Active subthreshold dendritic conductances  
672 shape the local field potential. *Journal of Physiology* 594 (13), 3809–3825.
- 673 Ness, T. V., Remme, M. W. H., Einevoll, G. T., 2018. h-Type Membrane Current Shapes the Local  
674 Field Potential from Populations of Pyramidal Neurons. *Journal of Neuroscience* 38 (26), 6011–  
675 6024.  
676 URL <http://www.jneurosci.org/lookup/doi/10.1523/JNEUROSCI.3278-17.2018>
- 677 NeuroEnsamble, 2017. Elephant - electrophysiology analysis toolkit.  
678 URL <https://github.com/NeuralEnsemble/elephant>
- 679 Nicholson, C., Freeman, J. A., 1975. Theory of current source-density analysis and determination of  
680 conductivity tensor for anuran cerebellum. *Journal of Neurophysiology* 38 (2), 356–368.
- 681 Nicholson, C., Syková, E., may 1998. Extracellular space structure revealed by diffusion analysis.  
682 *Trends in neurosciences* 21 (5), 207–15.  
683 URL <http://www.ncbi.nlm.nih.gov/pubmed/9610885>
- 684 Niederer, S., jan 2013. Regulation of ion gradients across myocardial ischemic border zones: a  
685 biophysical modelling analysis. *PLoS one* 8 (4), e60323.  
686 URL <http://www.ncbi.nlm.nih.gov/entrez/fetch?artid=3618345&tool=pmcentrez&rendertype=abstract>
- 688 Nunez, P. L., Srinivasan, R., 2006. *Electric Fields of the Brain*. Oxford University Press, New York.
- 689 Obien, M. E. J., Hierlemann, A., Frey, U., 2019. Accurate signal-source localization in brain slices by  
690 means of high-density microelectrode arrays. *Scientific Reports* 9 (1), 1–19.
- 691 O'Connell, R., Mori, Y., Oct 2016. Effects of glia in a triphasic continuum model of cortical spreading  
692 depression. *Bulletin of Mathematical Biology* 78 (10), 1943–1967.  
693 URL <https://doi.org/10.1007/s11538-016-0206-9>
- 694 Pettersen, K. H., Devor, A., Ulbert, I., Dale, A. M., Einevoll, G. T., Jun. 2006. Current-source density  
695 estimation based on inversion of electrostatic forward solution: effects of finite extent of neuronal  
696 activity and conductivity discontinuities. *Journal of neuroscience methods* 154 (1-2), 116–33.  
697 URL <http://www.ncbi.nlm.nih.gov/pubmed/16436298>
- 698 Pettersen, K. H., Einevoll, G. T., Feb. 2008. Amplitude variability and extracellular low-pass filtering  
699 of neuronal spikes. *Biophysical journal* 94 (3), 784–802.

- 700 URL <http://www.ncbi.nlm.nih.gov/pmc/articles/PMC2186261/>&tool=pmcentrez&rendertype=abstract
- 702 Pettersen, K. H., Hagen, E., Einevoll, G. T., Jun. 2008. Estimation of population firing rates and current source densities from laminar electrode recordings. *Journal of computational neuroscience* 24 (3), 291–313.
- 703 URL <http://www.ncbi.nlm.nih.gov/pubmed/17926125>
- 704
- 705 Pettersen, K. H., Lindén, H., Dale, A. M., Einevoll, G. T., 2012. Extracellular spikes and csd. In: Brette, R., Destexhe, A. (Eds.), *Handbook of Neural Activity Measurement*. Cambridge University Press, pp. 92–135.
- 706
- 707 Pettersen, K. H., Lindén, H., Tetzlaff, T., Einevoll, G. T., Nov. 2014. Power laws from linear neuronal cable theory: power spectral densities of the soma potential, soma membrane current and single-neuron contribution to the EEG. *PLoS computational biology* 10 (11), e1003928.
- 708 URL <http://www.ncbi.nlm.nih.gov/pmc/articles/PMC4230751/>&tool=pmcentrez&rendertype=abstract
- 709
- 710
- 711
- 712
- 713
- 714 Pfurtscheller, G., Cooper, R., 1975. Frequency dependence of the transmission of the EEG from cortex to scalp. *Electroencephalography and Clinical Neurophysiology* 38 (1), 93–96.
- 715
- 716 Pods, J., 2017. A comparison of computational models for the extracellular potential of neurons. *Journal of Integrative Neuroscience* 16 (1), 19–32.
- 717
- 718 Pods, J., Schönke, J., Bastian, P., Jul. 2013. Electrodiffusion models of neurons and extracellular space using the Poisson-Nernst-Planck equations—numerical simulation of the intra- and extracellular potential for an axon model. *Biophysical journal* 105 (1), 242–54.
- 719
- 720
- 721 URL <http://www.ncbi.nlm.nih.gov/pmc/articles/PMC3703912/>&tool=pmcentrez&rendertype=abstract
- 722
- 723 Potworowski, J., Jakuczun, W., Lęski, S., Wójcik, D., feb 2012. Kernel current source density method. *Neural computation* 24 (2), 541–75.
- 724
- 725 URL <http://www.ncbi.nlm.nih.gov/pmc/articles/PMC2209166/>
- 726
- 727 Ranck, J. B., 1963. Specific impedance of rabbit cerebral cortex. *Experimental Neurology* 7 (2), 144–152.
- 728 URL <http://www.sciencedirect.com/science/article/B6WFG-4GYGC4V-5/2-fb431eaa3c8ad95684a2c909cda91241>
- 729
- 730 Ranta, R., Le Cam, S., Tyvaert, L., Louis-Dorr, V., 2017. Assessing human brain impedance using simultaneous surface and intracerebral recordings. *Neuroscience* 343, 411–422.
- 731
- 732 Reimann, M. W., Anastassiou, C. A., Perin, R., Hill, S. L., Markram, H., Koch, C., jul 2013. A biophysically detailed model of neocortical local field potentials predicts the critical role of active membrane currents. *Neuron* 79 (2), 375–390.
- 733
- 734
- 735 URL <http://linkinghub.elsevier.com/retrieve/pii/S0896627313004431>

- 736 Savtchenko, L. P., Poo, M. M., Rusakov, D. A., 2017. Electrodiffusion phenomena in neuroscience:  
737 A neglected companion.  
738 URL <http://dx.doi.org/10.1038/nrn.2017.101>
- 739 Schomburg, E. W., Anastassiou, C. A., Buzsaki, G., Koch, C., aug 2012. The Spiking Component  
740 of Oscillatory Extracellular Potentials in the Rat Hippocampus. *Journal of Neuroscience* 32 (34),  
741 11798–11811.  
742 URL <http://www.jneurosci.org/cgi/doi/10.1523/JNEUROSCI.0656-12.2012>
- 743 Skaar, J.-E. W., Stasik, A. J., Hagen, E., Ness, T. V., Einevoll, G. T., 2020. Estimation of neural  
744 network model parameters from local field potentials (lfps). *PLoS Computational Biology*.
- 745 Solbrå, A., Bergersen, A. W., van den Brink, J., Malthe-Sørensen, A., Einevoll, G. T., Halnes, G.,  
746 2018. A Kirchhoff-Nernst-Planck framework for modeling large scale extracellular electrodiffusion  
747 surrounding morphologically detailed neurons. *PLoS Computational Biology* 14 (10), 1–26.
- 748 Srinivasan, R., Nunez, P. L., Silberstein, R. B., 1998. Spatial filtering and neocortical dynamics:  
749 estimates of eeg coherence. *IEEE transactions on Biomedical Engineering* 45 (7), 814–826.
- 750 Sterratt, D., Graham, B., Gillies, A., Willshaw, D., 2011. *Principles of computational modelling in*  
751 *neuroscience*. Cambridge University Press.
- 752 Suzuki, M., Larkum, M. E., 2017. Dendritic calcium spikes are clearly detectable at the cortical  
753 surface. *Nature Communications* 8 (276), 1–10.  
754 URL <http://dx.doi.org/10.1038/s41467-017-00282-4>
- 755 Teleńczuk, B., Dehghani, N., Le Van Quyen, M., Cash, S. S., Halgren, E., Hatsopoulos, N. G.,  
756 Destexhe, A., 2017. Local field potentials primarily reflect inhibitory neuron activity in human and  
757 monkey cortex. *Scientific reports* 7, 40211.
- 758 Tracey, B., Williams, M., 2011. Computationally efficient bioelectric field modeling and effects of  
759 frequency-dependent tissue capacitance. *Journal of Neural Engineering* 8 (3).
- 760 Wagner, T., Eden, U., Rushmore, J., Russo, C. J., Dipietro, L., Fregni, F., Simon, S., Rotman, S.,  
761 Pitskel, N. B., Ramos-Estebanez, C., Pascual-Leone, A., Grodzinsky, A. J., Zahn, M., Valero-  
762 Cabré, A., jan 2014. Impact of brain tissue filtering on neurostimulation fields: a modeling study.  
763 *NeuroImage* 85 (3), 1048–57.  
764 URL <http://www.ncbi.nlm.nih.gov/pubmed/23850466>
- 765 Zangiabadi, N., Ladino, L. D., Sina, F., Orozco-Hernández, J. P., Carter, A., Téllez-Zenteno, J. F.,  
766 2019. Deep brain stimulation and drug-resistant epilepsy: a review of the literature. *Frontiers in*  
767 *Neurology* 10.